Chemie der Erde 75 (2015) 375–387

Contents lists available at ScienceDirect

Chemie der Erde

journal homepage: www.elsevier.de/chemer

Petrology and geochemistry of the banded iron-formations from Ntem complex greenstones belt, Elom area, Southern Cameroon: Implications for the origin and depositional environment

Ganno Sylvestre[a,*], Ngnotue Timoleon[a,b], Kouankap Nono Gus Djibril[a,c], Nzenti Jean Paul[a], Notsa Fokeng Marianne[a]

[a] Department of Earth Sciences, University of Yaoundé I, P.O. Box. 3412 Messa, Yaoundé, Cameroon
[b] Department of Earth Sciences, University of Dschang, P.O. Box. 67, Dschang, Cameroon
[c] Department of Geology, HTTC, University of Bamenda, P.O.Box 39 Bambili, Bamenda, Cameroon

ARTICLE INFO

Article history:
Received 19 April 2015
Received in revised form 23 July 2015
Accepted 2 August 2015
Editorial handling - H.S. Moghadam

Keywords:
Banded iron-formation
Hydrothermal fluids
Seawater
Ntem greenstones belt
Cameroon

ABSTRACT

Banded iron-formations (BIFs) form an important part of the Archaean to Proterozoic greenstone belts in the Southern Cameroon. In this study, major, trace and REE chemistry of the banded iron-formation are utilized to explore the source of metals and to constraint the origin and depositional environment of these BIFs. The studied BIF belongs to the oxide facies iron formations composed mainly of iron oxide (mainly magnetite) mesobands alternating with quartz mesobands. The mineralogy of the BIF sample consists of magnetite and quartz with lesser amount of secondary martite, goethite and trace of gibbsite and smectite. The major element chemistry of these iron-formations is remarkably simple with the main constituents being SiO_2 and Fe_2O_3 which constitute 95.6–99.5% of the bulk rock. Low Al_2O_3, TiO_2, and HFSE concentrations show that they are relatively detritus-free chemical sediments. The Pearson's correlation matrix of major element reveals that there is a strong positive correlation ($r = 0.99$) of Al with Ti and no to weak negative correlation of Ti with Mn, Ca and weak positive correlation of Si with Ca, suggesting the null to very minor contribution of detrital material to chemical sediment. The trace elements with minor enrichments are transition metals such as Zn, Cr, Sr, V and Pb. This is an indicator of direct volcanogenic hydrothermal input in chemical precipitates. The studied BIF have a low ΣREE content, ranging between 0.41 and 3.22 ppm with an average of 0.87 ppm, similar to that of pure chemical sediments. The shale-normalized patterns show depletion in light REE, slightly enrichment in heavy REE and exhibit weak positive europium anomalies. These geochemical characteristics indicate that the source of Fe and Si was the result of deep ocean hydrothermal activity admixed with sea water. The absence of a large positive Eu anomaly in the studied BIF indicates an important role of low-temperature hydrothermal solutions. The chondrite-normalized REE patterns are characterized by LREE-enriched (Mean $La_{CN}/Yb_{CN} = 8.01$) and HREE depletion (Mean $Tb_{CN}/Yb_{CN} = 1.61$) patterns and show positive Ce anomalies. With the exception of one sample (LBR133), all of the BIF samples analyzed during this study have positive Ce anomalies on both chondrite- and PASS-normalized plots. This may indicate that the BIFs within the Elom area were formed within a redox stratified ocean. The positive Ce anomalies in the studied samples likely suggest that the basin in which Fe formations were deposited was reducing with respect to Ce, probably in the suboxic or anoxic seawaters.

1. Introduction

Banded iron-formations (BIF) are marine chemical precipitates that form an integral parts of the preserved Archaean to early Proterozoic sedimentary succession in different part of the world (Klein, 2005; Bhattacharya et al., 2007; Mloszewska et al., 2012). They are typically thinly banded or laminated and contain 15% or more iron of sedimentary origin, commonly but not necessarily containing layers of chert or quartz (James, 1954). According to Klein (2005), typical BIF consists of alternating Si- and Fe-rich layers within an evaluated total Fe and Si content of 20–40 wt.% and 43–56 wt.% respectively. More recently, Planavsky et al. (2010) have proposed the composition-based definition of Fe-formations as 'siliceous and Fe-rich sedimentary chemical precipitates with

* Corresponding author.
E-mail addresses: sganno2000@yahoo.fr, sganno@uy1.uninet.cm (G. Sylvestre).

http://dx.doi.org/10.1016/j.chemer.2015.08.001
0009-2819/

low levels of detrital siliciclastic or volcaniclastic material (<1% Al_2O_3) and greater than 10% total Fe, regardless of whether Fe is associated with a carbonate or oxide phase'. This definition of Fe formation encompasses both granular and banded Fe formations as well as ferruginous cherts (e.g. distal hydrothermal jaspers). Banded iron-formations occur in the geologic record from 3.8 Ga (Isua, West Greenland) to about 1.83.8 Ga with a maximal abundance at about 2.53.8 Ga, and a reoccurrence in Neoproterozoic time (from about 0.8 and 0.63.8 Ga; e.g. Rapitan iron-formation, Yukon, Canada; eg. Spier et al., 2007; Frei et al., 2008; Bekker et al., 2010; Basta et al., 2011). Although many aspects of their origin remains unresolved, it is widely accepted that secular changes in the style of their deposition are linked to the environmental and geochemical evolution of the earth (Bekker et al., 2010). Classically, two types of Precambrian iron formations have been recognized with respect to their depositional setting: (i) Algoma-type iron formations are in close proximity to ancient volcanic centers suggesting a sub-aqueous hydrothermal origin similar to modern day sea-floor spreading centers (Gross, 1983); (ii) the Lake Superior-type BIFs are developed in passive-margin sedimentary rock successions and generally lack direct relationships with extrusive volcanic materials and are therefore interpreted as chemical precipitates of iron-rich waters in a shallow sea (James, 1954).

In Cameroon, the Archaean greenstone belt crops in the southern part of the country within the Ntem complex which corresponds to the northern edge of the Congo craton. This craton, as other cratonic areas around the world, hosts many mineral deposits, some of which include iron ore with banded iron formation protore. The major iron ore deposits of the Congo craton include Avima, Boka Boka and Nabeba in Congo, Mitzic, Belinga and Minkebe in 3.8 Gabon and, Mbalam and Nkout deposits in Cameroon (Suh et al., 2008). The Elom greenstone belt forms part of the iron belt of the Archaean Ntem unit. This belt is characterized by the occurrence of banded-iron formations. The origin and genetic models of these formations are not precisely constrained, although the genetic model of a mineral deposit is fundamental for a more efficient mineral exploration plan. Few detailed studies on the Ntem Complex BIF have been carried out in the particularly on the high-grade iron ore Mballam deposit (Suh et al., 2008; Nforba et al., 2010; Chombong and Suh, 2013; Ilouga et al., 2013). This study presents petrographical and geochemical data on the Elom BIF from the Ntem greenstones belt in southern Cameroon. These data are used to characterize the iron-formations samples that are considered to represent the precursor of iron ore in order to place some constraints on the source of chemical components of these rocks and clarify their origin and depositional environments.

2. Geological setting

The Elom area is located within the Archean Ntem complex greenstones belt at the northwestern margin of the Congo craton (Maurizot et al., 1986; Nédélec et al., 1990; Goodwin, 1991), which is bordered in the north by the Yaounde Group (e.g. Nzenti et al., 1988; Barbey et al., 1990; Mvondo et al., 2003; Toteu et al., 2006), of the Pan-African orogenic belt in Central Africa (Fig. 1A). The Ntem complex is predominantly made up of Archaean rocks that were partially reworked during the Paleoproterozoic–Transamazonian cycle (Toteu et al., 1994; Tchameni et al., 2001). The greenstone formations are Mesoarchaean in age and include metagrewacke, banded-iron formations, sillimanite-bearing gneiss, and amphibolite, now preserved as xenolith in younger intrusive complexes (Shang et al., 2007; Shang et al., 2010). The intrusive complexes consist of charnockite and a variety other of rocks which define a TTG (tonalite–trondjemite–granodiorite) suite (Nédélec et al., 1990; Pouclet et al., 2007). Abundant gneissic and migmatitic structures in the TTG are indicative of late- to post-tectonic partial melting events between 2700 and 2500 Ma, which affected both the TTG and greenstone terranes (Kornprobst et al., 1976; Nédélec et al., 1990; Shang et al., 2001; Shang et al., 2010). The main structures in the Ntem complex are E–W-trending S_1 foliation and numerous granitic plutons that are usually emplaced along a SW–NE-tending S_2 foliation. The S_1 foliation dips steeply to the north and its locally deformed into mesoscopic isoclinal D_2 folds (Suh et al., 2009). The S_2 foliation is a regional, steeply dipping planar fabric with variably oriented stretching lineation and large scale open folds that are associated with N–S-trending sinistral and dextral strike-slip faults and S_3 mylonitic foliation. It has been suggested that the Ntem complex later underwent regional metamorphism associated to the Eburnean–Transamazonian orogeny (Toteu et al., 1994; Shang et al., 2004).

In the study area (Fig. 1B), banded iron-formations, high-K granites intruding TTG and cross-cutting dolerite dykes were identified (Maurizot et al., 1986; Shang et al., 2010). The doleritic magmatism has been dated as Late Archaean and interpreted as the heat source for remelting TTG and charnockites and generating high-K granites, thus suggesting the coeval nature of doleritic magmatism and high-K granite genesis in the Ntem complex (Shang et al., 2007, 2010). Banded-iron formations are the main lithology at Elom area. They form prominent ridges with NW–SE orientation and consist of rhythmically alternating fine bands of Fe-oxide and metachert metamorphosed into greenschist to amphibolite facies. The main prospect (Elom hill) is 11 km long and 0.5–2 km wide, but smaller size prospects also exist in the area. The BIF bands are folded and generally trend NW–SE to E–W with steeply dip (70–90°) towards the NE or SW and N, respectively.

3. Sampling and analytical methods

Samples were collected from several discontinuous outcrops of the Elom iron ore prospect, a mineral exploration property of Divine Mining Ltd. (Fig. 1B). Proper care was taken to collect the best possible fresh sample. Eight representative samples of banded-iron formations were investigated in terms of their mineral chemistry and whole rock geochemistry. Polished thin sections were prepared from representative samples at Geotech Lab (Vancouver, Canada) using conventional techniques. Mineral identification was attained by means of X-ray diffraction (XRD) and petrographic studies under both transmitted and reflected light. Chemical analysis was done using the pulp Whole-rock analyses were done by Inductively Coupled Plasma-Atomic Emission (ICP–AES) for major elements and by Inductively Coupled Plasma Mass Spectrometry (ICP-MS) for trace elements and REE at ALS Minerals Global Group, Vancouver (Canada). The samples were pulverized to obtain a homogeneous sample out of which 50–60 g was obtained for the analyses. 0.2 g of rock powder was fused with 1.5 g $LiBO_2$ and then dissolved in 100 mm^3 5% HNO_3. Analytical uncertainties vary from 0.1% to 0.04% for major elements; 0.1 to 0.5% for trace elements; and 0.01 to 0.5 ppm for rare earth elements. Loss on ignition (LOI) was determined by weight difference after ignition at 1000 °C. Various standards were used and data quality assurance was verified by running these standards between samples as unknowns. Analysis precision for rare earth elements is estimated at 5% for concentrations >10 ppm and 10% when lower.

4. Results

4.1. Petrography and ore mineralogy

The studied banded iron-formations crop as ridges (Fig. 2a) within their host rocks because they are resistant to weather-

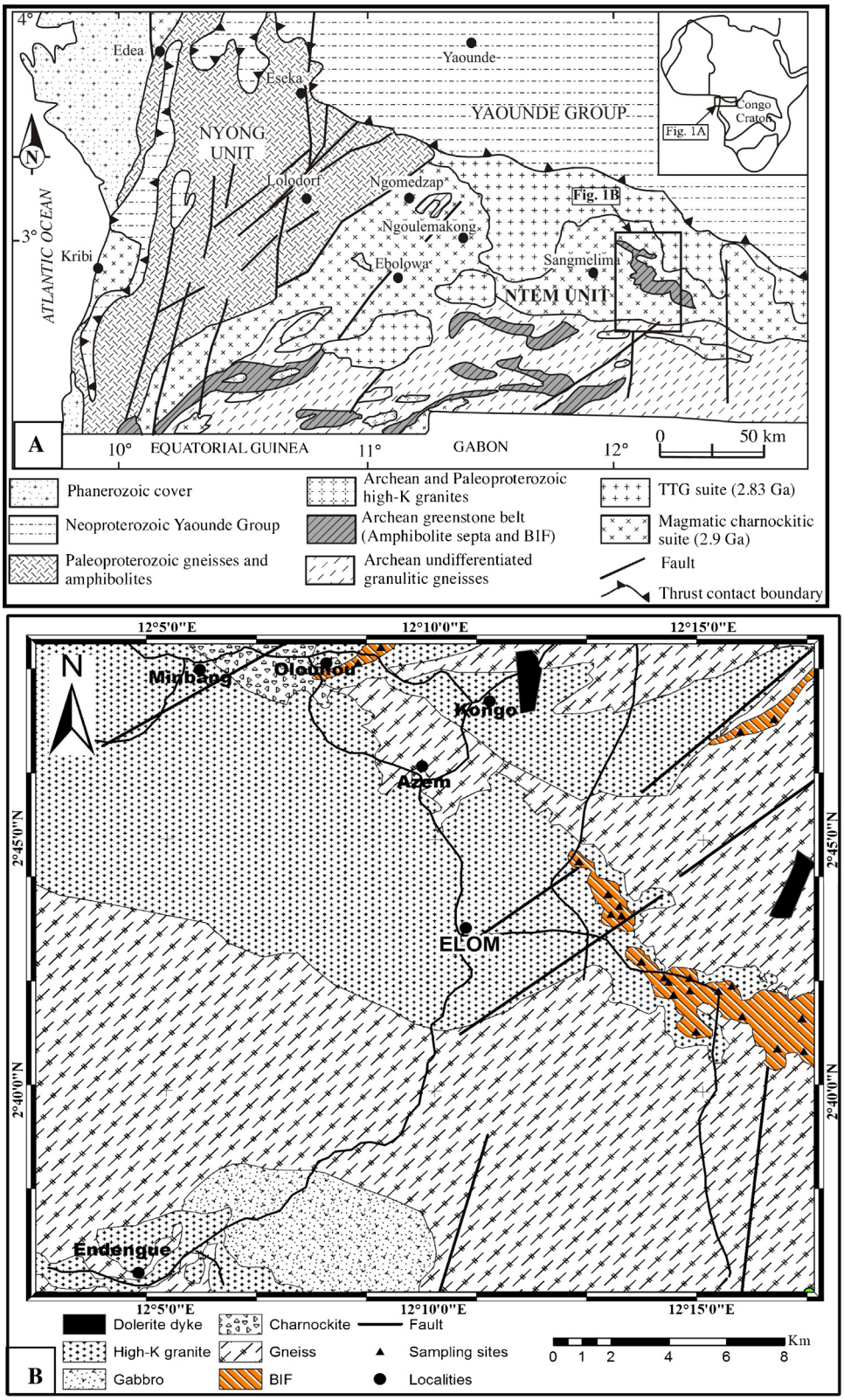

Fig. 1. (A) Simplified geological map of South-West Cameroun (Maurizot et al., 1986). (B) Detailed geological map of Elom area.

ing. They are well banded and showed alternation of silica-rich light bands and iron-rich dark grey to reddish bands (Fig. 2b). The BIF bands are generally parallel and their thickness varies from millimeter- to centimeter-scale (usually from 1 mm to 2 cm thick). The bands are commonly folded; exhibiting minor and major folds (Fig. 2c and d). The intense folding gives rise to repetition of the bands, increasing their thickness (Fig. 2c). The folding structures are asymmetric and display isoclinal to kink-band folds. The iron bands are well bedded, mesobanding is clearly observed especially when the gangue materials have a color different from that of

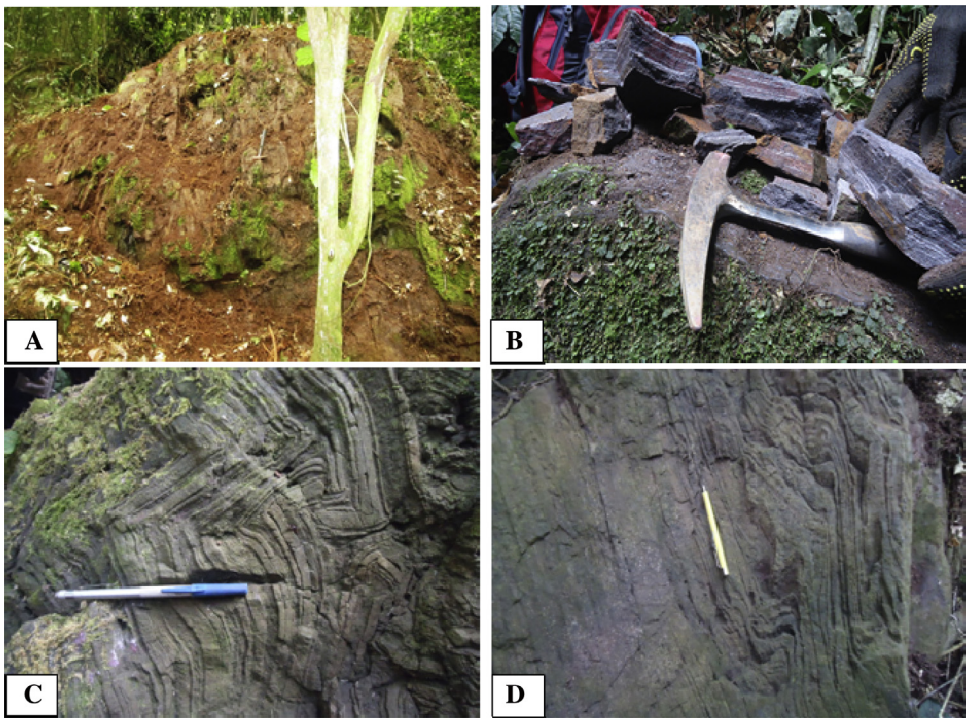

Fig. 2. Field observations of the studied BIF. (A) Dome shape exposure of BIF in Elom hill. (B). Outcrop and hand specimen pictures showing alternation of silica-rich light bands and iron-rich dark grey to reddish bands. (C and D) Highly folded bands exhibiting major (C) and minor (D) folding structures in BIF. (For interpretation of the references to color in this figure legend, the reader is referred to the web version of this article.)

the iron mesobands. In some outcrops, the iron mesobands have sharp straight contacts against the gangue mesobands. The studied lithology belongs to the oxide facies iron formations (James, 1954), composed mainly of iron oxide mesobands alternating with quartz mesobands. The mineralogy of the BIF sample consists of magnetite and quartz with lesser amount of secondary martite/hematite, goethite and trace of gibbsite and smectite (Fig. 3).

Magnetite forms either separate microbands or is mixed with quartz (Fig. 4a). It is present as euhedral and subhedral crystals, medium to coarse-grained. This coarse habit of the magnetite

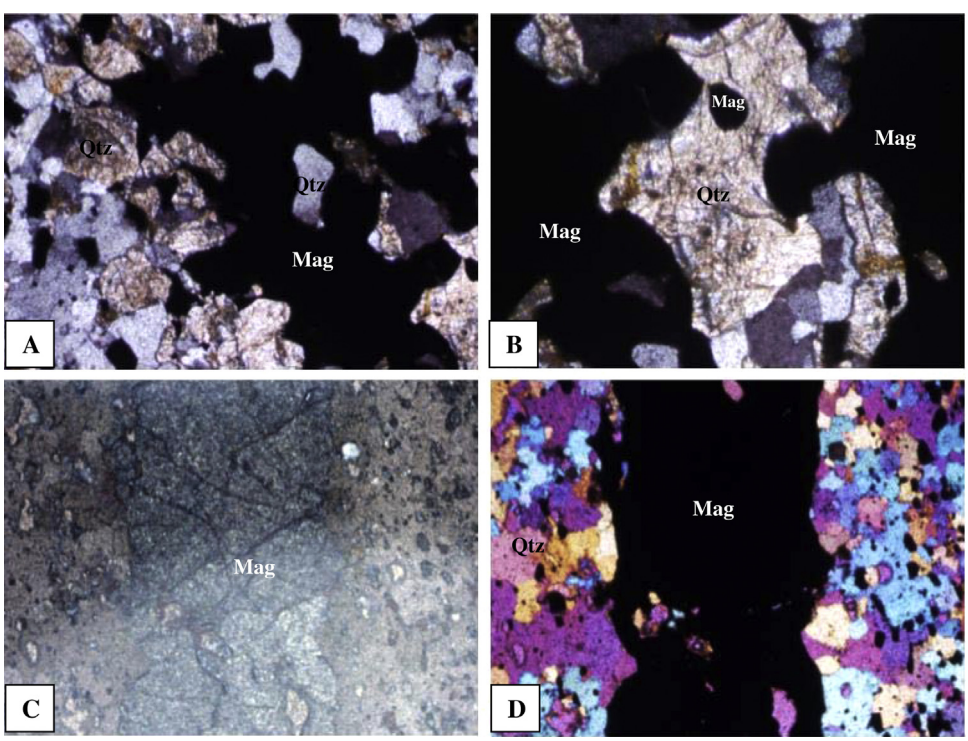

Fig. 3. Microscopic views of the studied BIF. (A) microbanding in the BIF consisting of alternations of magnetite-rich and silica-rich microbands, reflected light (field view = 1 mm across). (B) Detail view of magnetite-rich microband showing quartz in the matrix of iron oxide (field view = 0.4 mm across). (C and D) photomicrographs showing granoblastic-polygonal microstructure (Reflected (C) and Transmitted (D) light, field view = 1 mm across). Mag: magnetite; Qtz: quartz.

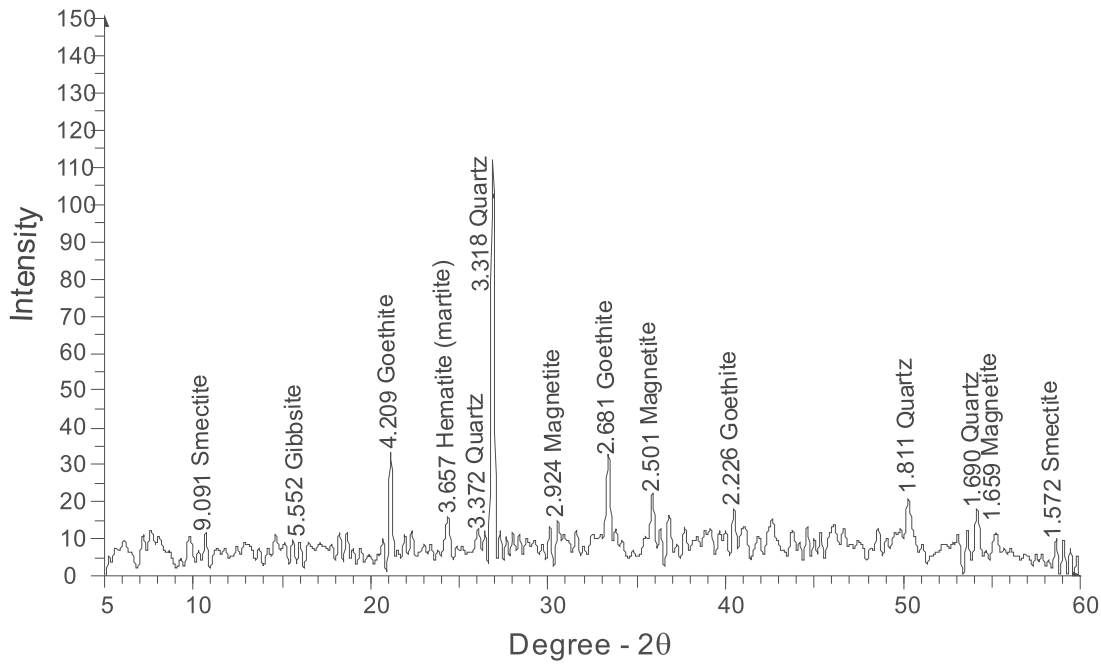

Fig. 4. X-ray diffraction spectra for bulk sample of BIF, indicating good peaks for quartz and magnetite, as well as geothite.

crystal is indicative for recrystallization and/or replacement under late diagenetic or metamorphic conditions. Most of the magnetite crystals display different degrees of martitization (Fig. 4c), probably related to the near-surface oxidation. Martite appears as subhedral grains with the trellis texture of the original magnetite. Geothite crystals resulting from hydration of magnetite are also present, as small isolated subhedral and xenomorphic crystals (Fig. 4d). Geothite, together with recrystallized quartz, fill the pores and intergranular spaces. Gibbsite and smectite are the weathering products.

The siliceous bands are essentially composed of quartz. Fine magnetite is also disseminated in such bands (Fig. 4c). Quartz is present as a matrix for the different iron oxide minerals in iron-rich bands. This mineral is also occurs as inclusions in magnetite. Quartz crystals are fine- to very fine-grained, with size variation from one band to another in the same sample. They display granoblastic-polygonal microstructure with intergranular triple junctions that suggest static recrystallization.

4.2. Geochemistry

4.2.1. Major oxides

The bulk geochemical composition (major elements) of eight representative samples of the Elom banded iron-formations is listed in Table 1. The major element chemistry of these iron-formations is remarkably simple with the main constituents being SiO_2 and Fe_2O_3 (all Fe expressed as Fe^{3+}). This is reflected in the overall mineralogy of the studied rocks composed mainly of iron oxide/hydroxyl mineral and quartz as shown from the petrography. These two elements (SiO_2 and Fe_2O_3) constitute 95.6–99.5% (mean: 98.17%) of the bulk of the banded iron-formations. SiO_2 and Fe_2O_3 contents are 32.13–0.02% and 52.49–65.09%, respectively. Fe_2O_3 contents are highest in samples with slight goethite alteration. There is a strong negative correlation ($r = -0.95$) between Fe_2O_3 and SiO_2, suggesting the incorporation of Fe_2O_3 and SiO_2 in different mineral phases. Al_2O_3 contents lie between 0.16 and 1.89% and show no to weak negative correlation with SiO_2 ($r = -0.08$) and

Table 1
Major element composition (wt.%) and element ratios of the Elom BIF.

Sample no.	LBR12	LBR16	LBR25	LBR53	LBR62	LBR107	LBR108	LBR133	Mean
Weight percent									
SiO_2	43.75	46.02	40.52	40.82	38.61	32.13	38.66	39.34	39.98
TiO_2	0.01	0.01	0.01	0.01	0.14	0.01	0.01	0.01	0.03
Al_2O_3	0.28	0.27	0.32	0.29	1.89	0.16	0.23	0.43	0.48
Fe_2O_3	55.75	52.49	57.30	57.60	56.99	65.09	60.20	60.13	58.19
MnO	0.03	0.03	0.03	0.10	0.07	0.07	0.09	0.09	0.07
MgO	0.02	0.01	0.07	0.06	0.02	0.01	0.06	0.23	0.06
CaO	0.01	0.03	0.01	0.04	0.01	0.01	0.01	0.04	0.02
Na_2O	0.01	0.01	0.01	0.01	0.01	0.02	0.02	0.02	0.01
K_2O	0.02	0.01	0.01	0.01	0.05	0.01	0.01	0.01	0.02
P_2O_5	0.07	0.04	0.17	0.08	0.09	0.03	0.06	0.10	0.08
LOI	0.04	1.08	1.55	0.97	2.11	2.46	0.65	-0.40	1.06
Total	100.00	100.00	100.00	100.00	100.00	100.00	100.00	100.00	100.00
Si/Al	153.57	168.52	127.74	142.50	20.43	204.67	171.36	91.43	135.03
Al/Ti	28.00	27.00	31.00	28.00	13.21	15.00	22.00	42.00	25.78
Fe/Ti	5480	5190	5600	5630	398.5714	6220	5870	5870	5032.32

Table 2
Pearson's correlation matrix for major element oxides.

	SiO_2	TiO_2	Al_2O_3	Fe_2O_3	MnO	MgO	CaO	Na_2O	K_2O	P_2O_5	LOI
SiO_2	1										
TiO_2	−0.14	1.00									
Al_2O_3	−0.08	0.99	1.00								
Fe_2O_3	−0.95	−0.13	−0.18	1.00							
MnO	−0.52	0.08	0.09	0.56	1.00						
MgO	−0.05	−0.23	−0.11	0.22	0.43	1.00					
CaO	0.30	−0.29	−0.21	−0.19	0.41	0.57	1.00				
Na_2O	−0.68	−0.29	−0.31	0.82	0.55	0.44	0.00	1.00			
K_2O	−0.05	0.97	0.96	−0.19	−0.03	−0.28	−0.36	−0.36	1.00		
P_2O_5	0.12	0.09	0.17	−0.16	−0.18	0.41	−0.05	−0.32	0.07	1.00	
LOI	−0.52	0.44	0.34	0.26	−0.09	−0.63	−0.47	−0.11	0.34	−0.09	1.00

Fe_2O_3 ($r = -0.18$). Relative elevated Al and Ti contents (1.89% and 0.14%, respectively) were observed in sample LBR62, suggesting trace inputs of detrital material. Na_2O and K_2O contents are very low in the studied samples. MnO (0.03–0.1%), MgO (0.01–0.23%) and CaO (0.01–0.04%) contents are significantly very low. The samples with relative elevated (compared to other samples) MgO contents show weak positive correlation with CaO, suggesting the incorporation of MgO in carbonate which is present as trace phase in mode. P_2O_5 contents range between 0.03 and 0.17%. From the Pearson's correlation matrix (Table 2), it is shown that there is a strong positive correlation ($r = 0.99$) of Al with Ti and no to weak negative correlation of Ti with Mn, Ca and weak positive correlation of Si with Ca. These correlations reflect the null to very minor contribution of detrital material to chemical sediment.

4.2.2. Trace elements

Concentrations of trace elements in the bulk samples are shown in Table 3. In terms of trace element composition, no significant enrichments were encountered. When compared to the average upper continental crust (Taylor and McLennan, 1985), the studied BIF are depleted in high field strength elements (Nb, U, Th, Zr, Hf, Pb, REE), and large ion lithophile elements (Sr, Rb). The trace elements with minor enrichments are transition metals such as Zn(0.23–1.12 ppm), Cr(3.11–4.28 ppm), Sr(0.05–0.46 ppm), V(0.81–1.06 ppm) and Pb(0.08–0.57 ppm). These elements are commonly used as indicators of direct volcanogenic hydrothermal input in chemical precipitates. In addition, Fe exhibits weak positive correlations with Zn and V pointing a hydrothermal source of these metals.

4.2.3. Rare earth elements

Rare earth element (REE) distributions in the bulk samples are shown in Table 3. The Elom Banded iron-formations have generally low absolute REE contents (0.41–3.22 ppm) similar to that of pure chemical sediments. These low values are typical of Archean iron formation (Fryer, 1983; Barrett et al., 1988). REE patterns, normalized to the Post-Archean Australian Shale (PAAS, subscript SN), of the selected samples of Elom BIF are depicted (Fig. 5). The degree of light REE (LREE) enrichment relative to heavy REE (HREE) is presented as the ratios of PAAS-normalized La and Yb (La/Yb), Tb and Yb (Tb/Yb). Eu anomalies are quantitatively defined as $Eu/Eu^* = Eu_N/(Sm_N \times Gd_N)^{1/2}$. When Eu is depleted, Eu/Eu* values are below unity. The REE patterns are characterized by a slight depletion in LREE (Mean $La_{SN}/Yb_{SN} = 0.86$) relative to HREE (Mean $Tb_{SN}/Yb_{SN} = 1.40$), apparent positive anomalies in both Eu and Ce. Evaluation of the presence or the absence of Ce anomaly is often complicated because of the anomalous behavior of La (Bau and Dulski, 1996). Lanthanum enrichment, together with the well-known Ce depletion has been identified in modern seawaters. Positive La anomalies have also been reported for hydrothermal Fe-Mn sediment on oceanic crust. Consequently, anomalous La

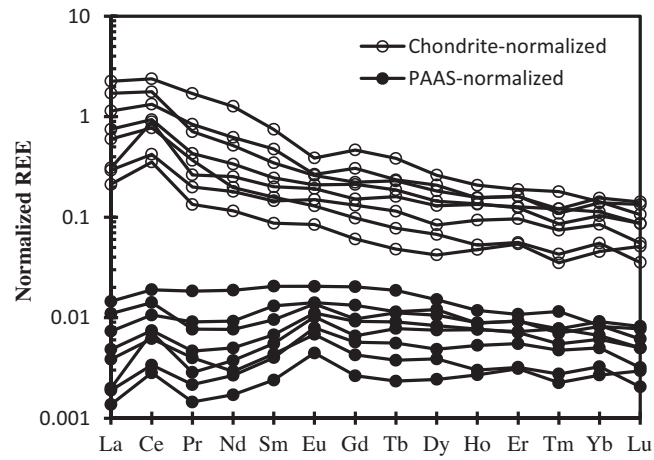

Fig. 5. REE patterns (PASS- and chondrite-normalized REE) of Elom BIF. Normalization value of PASS and chondrite after McLennan et al. (1993) and Boynton (1984), respectively.

enrichment can create 'false' negative Ce anomalies in some cases. In order to distinguish 'true' Ce anomalies from 'false' ones in BIF, plots of Ce/Ce* vs. Pr/Pr* has been used by many authors (eg. Bau and Dulski, 1996; Klein, 2005; Kato et al., 2006; Planavsky et al., 2010; Basta et al., 2011 and references therein). The Ce/Ce* and Pr/Pr* ratios are calculated as $Ce_{SN}/(La_{SN} \times Pr_{SN})^{1/2}$ and as $Pr_{SN}/(Ce_{SN} \times Nd_{SN})^{1/2}$, respectively. The Ce/Ce* vs. Pr/Pr* diagram of Elom BIF (Fig. 6) shows that the majority of samples have true positive Ce anomaly and only one sample (LBR133) has true negative Ce anomaly. The true positive cerium anomaly is a distinctive feature between Archaean to early Paleoproterozoic BIF and late Paleoproterozoic BIF (Planavsky et al., 2010)

The REE data were also plotted in chondrite normalized (subscript CN; Normalising values after Boynton, 1984) diagrams in Fig. 5. As proposed by Bau and Dulski (1996), chondrite-normalization has the advantage of illustrating the loss of the positive Eu anomaly at the Archaean/Proterozoic boundary. The chondrite-normalized REE patterns are fractionated. They are characterized by LREE-enriched (Mean $La_{CN}/Yb_{CN} = 8.01$) and slightly HREE depletion (Mean $Tb_{CN}/Yb_{CN} = 1.61$) patterns. The chondrite-

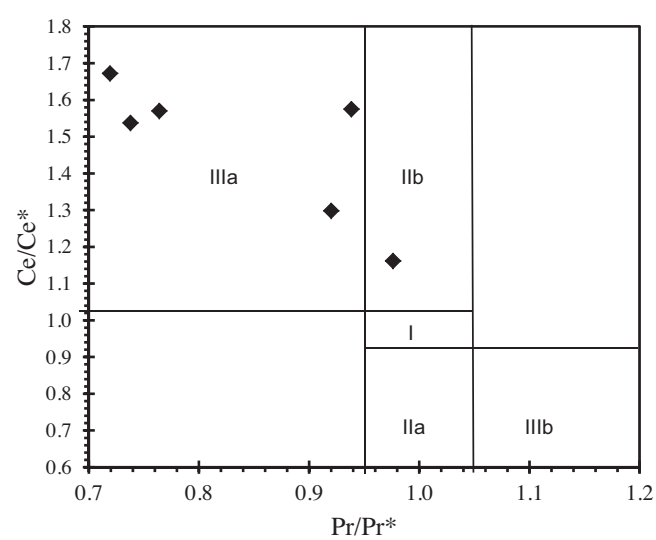

Fig. 6. $(Ce/Ce^*)_{SN}$ vs. $(Pr/Pr^*)_{SN}$ diagram (after Bau and Dulski, 1996) for the Elom BIF. Field I: neither Ce nor La anomaly; field IIa: positive La anomaly, no Ce anomaly; field IIb: negative La anomaly, no Ce anomaly; field IIIa: positive Ce anomaly; field IIIb: negative Ce anomaly.

Table 3
Trace and rare earth element compositions (ppm) and element ratios of BIF from Elom area.

Sample no.	LBR12	LBR16	LBR25	LBR53	LBR62	LBR107	LBR108	LBR133	Mean
Parts per million									
Zn	0.2300	0.2600	1.1200	0.4000	0.4800	0.2300	0.4200	0.4200	0.4450
Cu	<dl	0.0600	<dl	0.0900	0.1000	<dl	0.1000	0.0600	0.0513
Ni	<dl	<dl	<dl	<dl	0.0800	<dl	<dl	0.0600	0.0175
Co	0.0010	0.0550	0.0030	0.1490	0.1370	0.0020	0.1940	0.1800	0.0901
Cr	3.4700	3.9400	3.6500	3.8800	3.7300	3.1100	3.8300	4.0100	3.7025
V	0.8100	0.8900	0.8400	0.8700	0.8500	0.7700	0.9600	1.0000	0.8738
Cs	0.0031	0.0009	0.0010	0.0021	0.0067	0.0013	0.0024	0.0023	0.0025
Rb	0.1270	0.0310	0.0420	0.0270	0.1440	0.0140	0.1070	0.0650	0.0696
Sr	0.5320	0.1590	0.1960	0.1440	0.4040	0.0580	0.2000	0.3180	0.2514
U	0.0759	0.1160	0.0396	0.1675	0.0458	0.0314	0.0457	0.1225	0.0806
Th	0.2380	0.3780	0.2370	0.0621	0.0192	0.0671	0.0257	0.0272	0.1318
Pb	0.2180	0.5700	0.1870	0.3370	0.2020	0.1040	0.0830	0.3130	0.2518
Zr	0.0170	0.0210	0.0220	0.0060	0.0010	0.0070	0.0010	0.0010	0.0095
Y	0.1010	0.0758	0.2520	0.2150	0.2320	0.1890	0.1570	0.2690	0.1864
W	0.0040	0.0040	0.0060	0.0050	0.0050	0.0280	0.0230	0.0200	0.0119
La	0.1465	0.0519	0.1835	0.2790	0.4180	0.0718	0.0755	0.5520	0.2223
Ce	0.4940	0.2260	0.5960	0.8490	1.1300	0.2700	0.5670	1.5200	0.7065
Pr	0.0355	0.0129	0.0415	0.0810	0.0683	0.0192	0.0254	0.1640	0.0560
Nd	0.0936	0.0547	0.1600	0.2950	0.2450	0.0853	0.1200	0.6000	0.2067
Sm	0.0243	0.0134	0.0378	0.0733	0.0535	0.0224	0.0309	0.1150	0.0463
Eu	0.0075	0.0049	0.0122	0.0155	0.0151	0.0087	0.0112	0.0225	0.0122
Gd	0.0200	0.0124	0.0433	0.0625	0.0455	0.0268	0.0310	0.0953	0.0421
Tb	0.0029	0.0018	0.0070	0.0088	0.0086	0.0043	0.0060	0.0144	0.0067
Dy	0.0171	0.0107	0.0366	0.0530	0.0464	0.0213	0.0331	0.0666	0.0356
Ho	0.0030	0.0027	0.0077	0.0088	0.0089	0.0053	0.0076	0.0118	0.0070
Er	0.0093	0.0090	0.0206	0.0269	0.0266	0.0160	0.0211	0.0313	0.0201
Tm	0.0011	0.0009	0.0022	0.0028	0.0031	0.0019	0.0031	0.0046	0.0025
Yb	0.0091	0.0075	0.0171	0.0229	0.0256	0.0140	0.0186	0.0235	0.0173
Lu	0.0009	0.0013	0.0022	0.0034	0.0036	0.0014	0.0022	0.0027	0.0022
Y/P_2O_5	1.4182	1.8738	1.4487	2.6268	2.5239	6.0203	2.5515	2.6260	2.6361
Co/Zn	0.0043	0.2115	0.0027	0.3725	0.2854	0.0087	0.4619	0.4286	0.2220
Eu/Sm	0.3086	0.3657	0.3228	0.2115	0.2822	0.3884	0.3625	0.1957	0.3047
Y/Ho	33.6667	28.0741	32.7273	24.4318	26.0674	35.6604	20.6579	22.7966	28.0103
$(La/Yb)_{SN}$	1.1862	0.5099	0.7907	0.8977	1.2031	0.3779	0.2991	1.7308	0.8744
$(Tb/Yb)_{SN}$	1.1588	0.8727	1.4886	1.3974	1.2216	1.1169	1.1730	2.2282	1.3322
$(Eu/Eu^*)_{SN}$	1.5867	1.7729	1.4064	1.0680	1.4274	1.6561	1.6878	1.0024	1.4510
$(Pr/Pr^*)_{SN}$	0.9385	0.6596	0.7640	0.9201	0.7380	0.7192	0.5536	0.9763	0.7837
$(Ce/Ce^*)_{SN}$	1.5747	2.0078	1.5700	1.2983	1.5374	1.6717	2.9764	1.1613	1.7247
ΣREE	0.8648	0.4101	1.1677	1.7819	2.0982	0.5684	0.9527	3.2237	1.3834

dl: detection limits.

normalized patterns also exhibit Ce positive anomaly, similar to the Ce behavior on shale-normalized plot. However, Eu behavior in chondrite-nornalized REE is quite different from that of the shale-normalized pattern, exhibiting negative to slightly positive Eu anomaly (Eu/Eu*: 0.65–1.16). This decrease suggests a declining hydrothermal input into a deep ocean basin from Early Archean to Early Proterozoic time. Bau and Möller (1993) concluded that the decrease in the positive Eu anomaly is the result of the lowering of the temperature of the hydrothermal solutions, as a reflection of decreasing upper mantle temperature. As the size of the positive Eu anomaly of BIF decrease with age (Derry and Jacobsen, 1990; Bau and Dulski, 1996; Kato et al., 1998, 2006), the loss of positive Eu anomaly on the chondrite-normalized patterns is indicative for Paleoproterozoic age of the studied BIF. Also the chondrite-normalized REE patterns differ from the HREE-enriched trends ($Sm_{CN}/Yb_{CN} < 1$) which characterized most Archaean BIF (eg. Bau and Möller, 1993).

5. Discussion

5.1. Source of chemical components

The composition of Archaean chemical sediments ought to reflect input of solutes from both crustal weathering and hydrothermal emissions. Detrital input can also occur in shallow water facies iron formations, and such clastic particles tend to obscure the seawater signal. Identification of a detrital component in BIF was done mainly through elevated concentrations of Al_2O_3, TiO_2 and high field strength elements—HFSE (e.g., Zr, Hf, Ta, Th) as well as through co-variations between HFSE and REE ratios (La/La*, Y/Ho, Pr/Yb, Ce/Ce*—McLennan et al., 1993; Bau, 1993; Bolhar et al., 2004). Pure chemical sediments are enriched in Mn and Fe, but addition of detrital or volcanic material causes their dilution and enrichment of Ti, Al and Zr (Bonatti, 1975). High contents of SiO_2 and Fe_2O_3 in the studied banded iron-formations indicate the purity of the chemical precipitates. Low Al_2O_3 content of the banded iron-formations (0.15–0.42 wt.%; except sample LBR62 with Al_2O_3 content of 1.85%) further attests to the detritus-free nature of the silica-iron precipitates. Very small to undetectable Na_2O and K_2O contents may further indicate that contamination by pyroclastic debris was minimum during the precipitation of the banded iron-formations. However, a correlation matrix data shows that there are weak to significant positive correlations ($r = 0.45–0.96$) of Al with Ti, K, Rb and Sr indicating sedimentary inputs of siliciclastic material to chemical sediments (Ewers and Morris, 1981; Klein and Beukes, 1993; Manikyamba and Naqvi, 1995); but the weak negative correlation of Si with Al, Ti, La, Ce and low ΣREE content indicates that the detrital input was trivial. Thus the chemical components of Elom BIF have been formed predominantly by chemical precipitation processes.

5.2. Origin of Elom BIF

Most authors agree that BIFs are chemical sediments formed by precipitation of iron and silica from solutions consisting of a mixture of seawater with hydrothermal fluids. The main impurities are terrigenous sediments carried by rivers or winds, or deposited by volcanic activity (Klein and Beukes, 1989; Isley, 1995; Kato et al., 1998) or pelagic sediments (Lascelles, 2007). Although controversies remain regarding the origin of Fe and Si in BIFs, most workers consider that these components, together with Mn and a very low amount of trace elements, are derived from the leaching of basalt and komatiites of the ocean floor by hydrothermal fluids (e.g., Dymek and Klein, 1988; Beukes and Klein, 1990; Shimizu et al., 1990; Klein and Beukes, 1992; Bau and Möller, 1993; Kato et al., 1998). Only a few authors attribute the origin of Fe and Si to the weathering of continental rocks (e.g., Holland, 1984; Manikyamba et al., 1993; Kholodov and Butuzova, 2001). This is because BIFs and deep hydrothermal deposits have the same REE signature, characterized by positive Eu anomalies and depletion of LREE (Derry and Jacobsen, 1990; Danielson et al., 1992). The patterns of element abundances preserved in ancient chemical sediments can be used to constrain the influence of seawater, hydrothermal, biogenic and detrital sources on the sediment composition (Lottermoser and Ashley, 2000). Proposed methods for distinguishing between seawater, hydrothermal, biogenic and detrital sources are based on differences in the mineralogical, chemical and isotopic composition. The Si/Al ratio is commonly used to detect eventual hydrogenous, respectively hydrothermal material supply. It is worth underlining here that the Si/Al ratio has been used to distinguish between hydrothermal Fe–Mn crusts, rich in Si and characterized by a Si/Al ratio >5.1, and hydrogeneous Fe-deposits (nodules), whose typical Si/Al ratio is 3, the same as marine sediments. The average Si/Al ratio of the studied BIF is 135 pointing to the hydrothermal origin of the studied BIF.

Bonatti (1975) suggested that hydrothermal metal-rich deposits could be distinguished from hydrogenous deposits formed by diagenetic processes on the basis of the relative abundance of SiO_2 and Al_2O_3. In this diagram (Fig. 7), the studied rocks are plotted within the hydrothermal field. Pure hydrothermal deposits contain very little Al and have high Al/Ti ratios (Marchig et al., 1982). Contamination of such deposits by pelagic and terrigenous deep-sea sediments enriches them in components such as Ti and Al, resulting drastic lowering of the Fe/Ti ratios and increase in the Al/(Al + Fe + Mn) ratio. On an Fe/Ti vs. Al/(Al + Fe + Mn) diagram of Barrett (1981), most of the studied BIF samples cluster on the hydrothermal Red Sea deposits and only one sample plots at the end of a mixing curve between hydrothermal deposits, as represented by metal-rich sediments of the East Pacific Rise (13°N and 21°N), and pelagic sediment (Fig. 8). This suggests that the major components (>90 %) of the Elom BIF are predominantly of hydrothermal origin. A predominantly hydrothermal origin is also consistent with the low Y/P_2O_5 ratios which fall in the 20–36 (average 28), similar to the ratios expected in pure hydrothermal deposits but lower than >100 found in pelagic and hydrogenous deposits (Marchig et al., 1982).

The lower contents of detrital-derived elements such as Y, Nb, and Zr in the Elom BIF as well as the relative null correlations between Al_2O_3 and these elements (Fig. 9A) support the previous conclusion from the major oxide distributions that the studied BIF are purely chemical sediments with little to no detrital input. ΣREE contents show also null correlations ($r^2 = 0.16$) with the Al_2O_3 contents (Fig. 9B) suggesting no detrital contribution to these rare earth elements.

The use of REE to constrain the origin of BIF and other Fe formations has been proposed by many authors (Bau and Dulski, 1999; Lottermoser and Ashley, 2000; Frei et al., 2008; Planavsky et al., 2010; Basta et al., 2011 and references therein). At the heart of REE studies in iron formation is the assumption that there is minimal fractionation of REE during precipitation of ferric iron oxides and oxyhydroxides (Bekker et al., 2010). The REEs in iron oxide-rich sediments appear to be rock buffered under most early- to late-stage diagenetic and metamorphic alteration conditions (Bau, 1993). Hence, iron formations are likely to preserve their primary REE pattern during burial and exhumation. The REE contents of the studied BIF are very low and the Shale-normalized patterns display both positive Ce and Eu anomalies. Possible source materials of the positive Eu anomaly of BIFs have been attributed to a hydrothermal solution (Campbell et al., 1988) and/or detrital feldspar. Because the $A1_2O_3$ contents of studied BIFs are very low (0.15–0.42 wt.%), the positive Eu anomaly of BIFs was not caused by detrital feldspar but by a hydrothermal solution.

With regard to the rare earth elements, hydrogenous deposits show high ΣREE, while the ΣREE of hydrothermal deposits are significantly lower (Hein et al., 1990; Usui and Someya, 1997). In this regard, the Elom BIFs have significantly low ΣREE (average of 0.87 ppm). This very low concentration of ΣREE is characteristic of hydrothermal source of the studied ores.

Furthermore, hydrothermal solutions have a near chondritic Y/Ho ratio (27), while that for seawater is superchondritic (Bau and Dulski, 1999). Bolhar et al. (2004) proposed that as terrestrial material (i.e., felsic and basaltic crust) has a constant Y/Ho ratio of ~26, smaller admixtures of any contaminant to chemical sediments precipitated from seawater would depress seawater-like superchondritic Y/Ho ratios (>44) and that co-variation would arise between Y/Ho and insoluble elements such as Zr with smaller admixture of any contaminant. The average Y/Ho ratio of the Elom BIF is 28.01, which is similar to the hydrothermal solution ratio and could suggest a hydrothermal source of the studied ores. The weakly positive correlation ($r = 0.39$) between Zr and Y/Ho for Elom BIF implies that the Y/Ho ratios in the original BIF precipitate did not experience significant changes because the amounts of detrital contaminants (as indicated by lowest Zr contents) were trivial.

According to Michard et al. (1983), Mitra et al. (1994), and Douville et al. (1999), hydrothermal solutions are produced by both high-temperature (>300 °C) and low-temperature (<200 °C) hydrothermal alteration of the oceanic crust. High-temperature hydrothermal alteration produces fluids with a pronounced positive Eu anomaly; whereas fluids produced by low-temperature hydrothermal alteration have a weak or no Eu anomaly (Michard et al., 1993). Bau and Dulski (1996) suggested that HREE-enrichment in Precambrian BIF are signals inherited from marine surface water, while positive Eu_{SN} anomalies are signals inherited from marine bottom water through the contribution of hydrothermal solutions.

The REE patterns for the studied BIFs can be produced by mixing of low-temperature hydrothermal solutions and seawater. HREE-enrichment ($Tb_{SN}/Yb_{SN} = 1.40$) relative to LREE ($La_{SN}/Yb_{SN} = 1.33$) in these BIFs is a feature inherited from seawater, while the small positive Eu anomaly ($Eu/Eu^* = 0.99–1.86$) is inherited from low-temperature hydrothermal solutions. Thus the REE patterns of the Elom BIF bear the characteristics of both hydrothermal solutions and seawater, similar to other BIFs (Bau and Dulski, 1996; Bolhar et al., 2005). The average Eu anomaly value of present-day hydrothermal solutions from the East Pacific Rise is reported to be 0.86 (Michard and Albarède, 1986). Modern hydrothermal iron-rich sediments from the East Pacific Rise have a consistent variety of Eu anomaly value from 0.03 (proximal) to 0.14 (distal) (Olivarez and Owen, 1991), which suggests that the Eu anomaly value of hydrothermal sediments is also affected by a strong and continuous overprinting of seawater-derived REEs. On the other hand, Barrett et al. (1988) have proposed that HREE-enrichment in PASS-normalized patterns for some iron formations associated with volcanic rocks is possibly inherited from a mafic volcanic

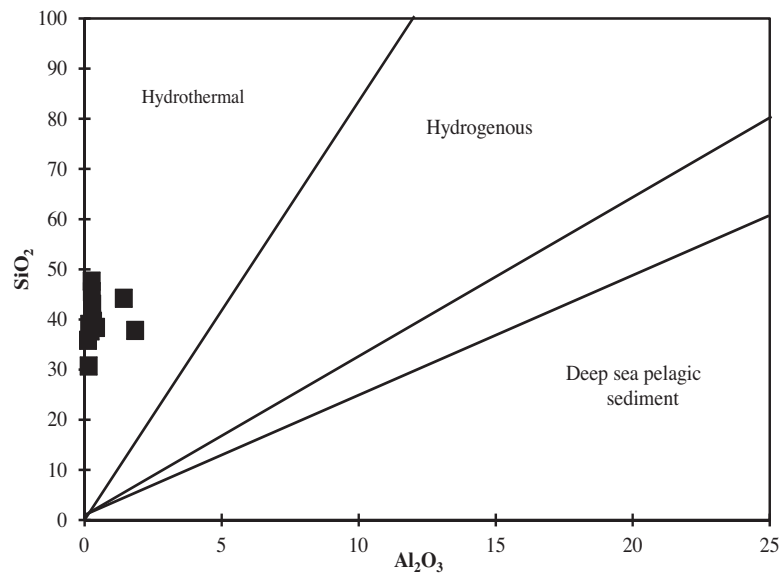

Fig. 7. SiO_2 vs. Al_2O_3 discrimination diagram indicating the hydrothermal affinity of the studied BIF.

source, following relatively low-temperature seawater rock interaction.

5.3. Environmental conditions

Precambrian BIFs formed during chemical precipitation from the ocean, and therefore their REE composition can be used to determine the geochemistry of seawater during BIF formation; this information can in turn be used to determine the redox state of the atmosphere and ocean at this time (Planavsky et al., 2010; Hou et al., 2014). Ce anomalies are considered to be indicative of an oxygenated hydrosphere (Kerrich et al., 2013). The studied BIFs do not show negative Ce anomalies (except sample LBR133) (Fig. 6), and most samples have positive Ce anomalies. Planavsky et al. (2010)

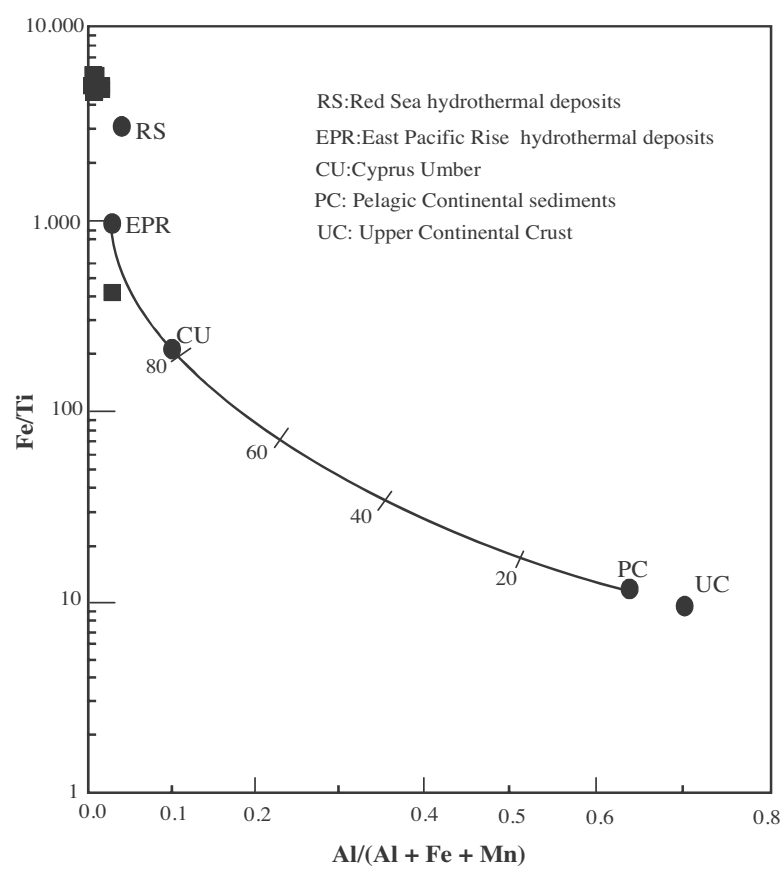

Fig. 8. Fe/Ti vs. Al/(Al + Fe + Mn) diagram of Elom BIF. The curve represents mixing of East Pacific Rise deposits (EPR) with pelagic sediments (PC) whereas the numbers indicate the approximate percentage of EPR in the mixture (adopted from Barrett, 1981). Also indicated are compositions for mean upper continental crust (UC, Taylor and McLennan, 1985), Red Sea hydrothermal deposits (RS, Marchig et al., 1982) and the Cyprus umber (CU).

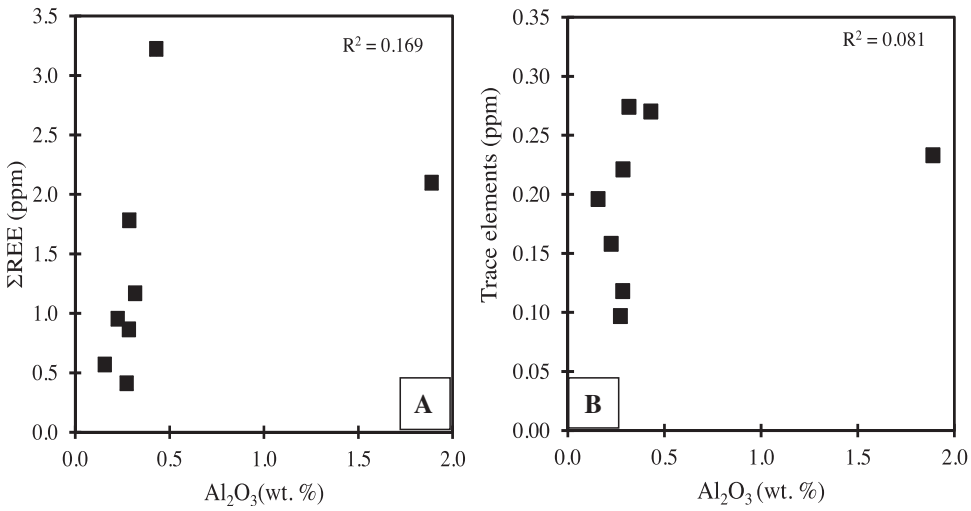

Fig. 9. (A) Detrital trace elements (Nb, Y, and Zr) vs. Al_2O_3 showing relative null correlations between Al_2O_3 and these elements; (B) Null correlations between Al_2O_3 and the ΣREE in the bulk samples of the studied BIF.

suggested a link between the lack of Ce anomalies within Paleoproterozoic BIFs and the Great Oxidation Event (GOE), primarily as positive Ce anomalies within BIFs are a result of redox reactions in the ancient ocean. If an area of ocean is not totally oxidized, the Ce, LREE, and Ho in solution are oxidized and are preferentially adsorbed by Mn and Fe hydroxides within oxidized surface waters; in comparison, the reductive dissolution of these precipitates in oxidation–reduction transition zones or in deeper waters would release Ce, LREE, and Ho into the seawater column (Planavsky et al., 2010). As seen in some modern basins (de Baar et al., 1988; Bau et al., 1997; De Carlo and Green, 2002), the dissolution of these metal oxyhydroxides would at times have led to the formation of positive dissolved Ce anomalies in deeper, anoxic–suboxic waters. Positive Ce anomalies would be transferred to the sedimentary record when Fe oxyhydroxide precipitation occurred in these suboxic or anoxic waters. Positive Ce anomalies in studied samples likely indicate a dissolved positive Ce anomaly, given that experimental work suggests (in contrast to Mn oxides) that minimal or no preferential Ce scavenging onto Fe oxyhydroxides occurs in the pH range relevant to marine conditions (Koeppenkastrop and De Carlo, 1992; Bau, 1999). These BIFs have an average Y/Ho ratio of 28, significantly lower than the Archean-Early Paleoproterozoic BIFs (average Y/Ho ratio of 39), and the Late Paleoproterozoic BIFs (average Y/Ho ratio of 32; Planavsky et al., 2010). However, these samples are LREE-depleted and HREE-enriched, similar to the Archaean and Early Paleoproterozoic BIFs. This result suggests the contemporaneous deposition of Elom BIF with the change in oxidation–reduction status of seawater, probably during the GOE.

5.4. Comparative petrography and geochemistry

The mineral assemblages described in the petrographic section are typical of oxide facies banded iron-formations encountered around the world (eg. James, 1954; Beukes, 1973; Klein, 2005; Bhattacharya et al., 2007). In Cameroon, BIF are mainly of oxide facies with either hematite or magnetite as dominant mineral. Comparing the Elom BIF with other BIF occurrences within the same Precambrian Iron Ore Belt in South Cameroon, the former are mainly magnetite-rich similar to the Ngoa iron ore deposit (Njinchuki, 2011). These deposits are different from the Metzimevin, Njweng (Mballam) and Nkout iron deposits composed predominantly of hematite and martite with monazite, apatite and pyrite as minor phases (Suh et al., 2008; 2009; Ilouga et al., 2013; Nsoh et al., 2014). Moreover, Ilouga et al. (2013) have described silicate facies BIF at Njweng prospect in the Mballam iron ore deposit. These types of BIF were not encountered in the Elom area. In terms of bulk-rock geochemistry, the Elom banded iron-formations show slightly elevated Fe_2O_3 and depressed SiO_2, TiO_2, MgO, MnO, CaO, Na_2O, K_2O and P_2O_5 values compared to average chemical compositions of other banded iron-formations occurrences in Proterozoic and Archean supracrustal belts (Fig. 10A). On this plot, it is observed that there is a significant variation in MgO, MnO, CaO, Na_2O and K_2O proportions which are very low in the study area BIF, whereas Fe_2O_3 contents are slightly enriched. The average concentrations of MnO (0.06) and P_2O_5 (0.08) of studied BIF show similarity with MnO and P_2O_5 (0.07) of Orissa oxide facies (Bhattacharya et al., 2007), but it is slightly higher than that of superior type (0.06). Also, the Al_2O_3 (0.47) contents in the Elom BIF are close to the Al_2O_3 contents in the Orissa BIF (0.35) and high to the Al_2O_3 contents of the Hotazel BIF (Tsikos and Moore, 1997). Small variations in Al_2O_3, K_2O and Na_2O_3 in the various banded iron-formations indicate the presence of various amounts of iron-rich silicate minerals. The studied BIF are markedly depleted in Zn Cu, Ni Co and V (Fig. 10B). Similar transition metals contents were encountered in both Hotazel and other Superior-type banded iron-formations. According to Gross and McLeod (1980), the depletion of transition metals constitutes a distinguishing feature between banded iron-formation that is genetically unrelated to volcanic activity and typical volcanogenic Algoma-type banded iron-formation.

The Elom BIF are depleted in REE which is consistent with the REE data of Archaean iron-formations elsewhere; but their REE concentrations are markedly depleted (ΣREE = 1.38 ppm) compared to other Archaean to Proterozoic oxide facies BIF of the world (Klein, 2005; Planavsky et al., 2010). The PASS-normalized REE patterns of the study area show slightly positive Eu anomalies ($Eu/Eu^* = 1.45$) and HREE-enriched trend ($Tb_{SN}/Yb_{SN} = 1.33$) similar to the REE patterns of other Archaean BIF, but differ from the latter by the slightly positive Ce anomalies ($Ce/Ce^* = 1.72$) similar to Gunflint and Biwabik, iron-formations, Animikie Basin, USA and Canada (Planavsky et al., 2010). The positive Ce anomalies characterizes late Paleoproterozoic (1.93.8 Ga) banded iron-formations (Planavsky et al., 2010). Fryer (1977) suggested that Eu/Sm ratio can be used to distinguished the Archaean (0.40–1.22) and Proterozoic (0.24–0.40) BIF. The Eu/Sm ratio of studied BIF ranges from 0.19 to 0.38. Although previous works have clearly shown that the greenstone terranes of Ntem complex are Mesoarchaean in age (Shang et al., 2010), the true positive Ce anomalies together with the Eu/Sm ratio of the studied BIF suggest their precipitation during late Pale-

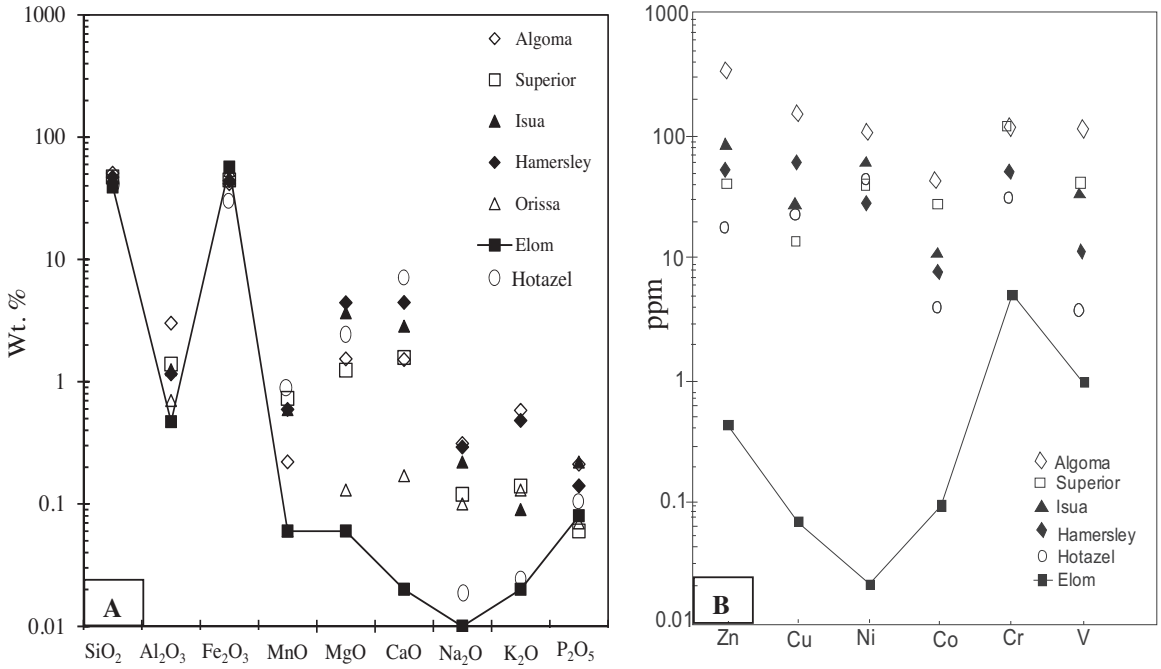

Fig. 10. Plot of average major elements concentrations (A) and transition metal values (B) of Elom BIF ($n = 8$) and other well studied banded iron-formations around the world.

oproterozoic time. In spite of the above REE behavior, the Elom BIF show most similarity with Lake Superior-type banded iron formations.

6. Conclusions

Representative BIF samples from the Elom area of the Ntem complex (southern Cameroon) were analyzed for their major, trace, and rare earth elements to clarify the origin of Fe-formations. The studied BIFs belong mainly to the oxide facies being composed of magnetite, microcrystalline quartz and secondary martite and geothite. Low Al_2O_3, TiO_2, Y, Nb, Zr and Th concentrations in most of the BIF samples suggest detritus-free chemical sediments. The high Si/Al ratio (average of 135) of the studied BIF suggests the hydrothermal origin. The Fe/Ti vs. Al/(Al + Fe + Mn) binary diagram supports this interpretation through the plot of all data in the hydrothermal Red Sea deposits field. On the other hand, the low ΣREE concentrations, the near chondritic Y/Ho ratio and the REE patterns for the studied BIF carry the signals of both hydrothermal solutions and seawater. HREE-enrichment is a signature inherited from seawater, whereas a positive Eu anomaly is a feature inherited from bottom water carrying a hydrothermal signature. The absence of a large positive Eu anomaly in the studied BIF indicates an important role of low-temperature hydrothermal solutions. Positive Ce anomalies in studied samples likely indicate a dissolved positive Ce anomaly, suggesting that the basin in which Fe formations were deposited was reducing with respect to Ce, probably in the suboxic or anoxic seawaters.

Acknowledgements

We gratefully acknowledge the mineral exploration company 'Divine Mining SA' for their permission to work within their permit area and for the logistic support during the field trip. We also thank Dr. Gideon Lambiv, University of Alberta, Canada, for his support in the reflected and transmitted light microphotographs. The paper was improved by the comments of two anonymous reviewers. The authors are indebted to Alexander Deutsch and Hadi Shafaii Moghadam for the constructive and helpful editorial handling of the manuscript. This is the contribution to ICGP-Y 616 project.

References

Barbey, P., Macaudière, J., Nzenti, J.P., 1990. High pressure dehydration melting of metapelites: evidence from migmatites of Yaounde (Cameroon). J. Petrol. 31, 401–427.

Barrett, T.J., 1981. Chemistry and mineralogy of Jurassic bedded chert overlying ophiolites in the North Appenines, Italy. Chem. Geol. 34, 289–317.

Barrett, T.J., Fralick, P.W., Javris, I., 1988. Rare-earth element geochemistry of some Archean iron formations north of Lake Superior, Ontario. Can. J. Earth Sci. 25, 570–580.

Basta, F.F., Maurice, A.E., Fontbote, L., Favarger, P., 2011. Petrology and geochemistry of the banded iron formation (BIF) of Wadi Karim and Um Anab, Eastern Desert, Egypt: implications for the origin of Neoproterozoic BIF. Precambrian Res. 187, 277–292.

Bau, M., Dulski, P., 1996. Distribution of yttrium and rare-earth elements in the Penge and Kuruman Iron Formation, Transvaal Supergroup, South Africa. Precambrian Res. 79, 37–55.

Bau, M., 1999. Scavenging of dissolved yttrium and rare earths by precipitating Fe oxyhydroxide: experimental evidence for Ce oxidation, Y–Ho fractionation, and lanthanide tetrad effect. Geochim. Cosmochim. Acta 63, 67–77.

Bau, M., Hohndorf, A., Dulski, P., Beukes, N.J., 1997. Sources of rare-earth elements and Fe in paleoproterozoic iron-formations from the Transvaal Supergroup, South Africa: evidence from neodymium isotopes. J. Geol. 105, 121–129.

Bau, M., Möller, P., 1993. Rare earth element systematics of the chemically precipitated component in Early Precambrian iron-formations and the evolution of the terrestrial atmosphere–hydrosphere–lithosphere system. Geochim. Cosmochim. Acta 57, 2239–2249.

Bau, M., 1993. Effects of syn- and post-depositional processes on the rare-earth element distribution in Precambrian iron-formations. Eur. J. Mineral. 5, 257–267.

Bau, M., Dulski, P., 1999. Comparing yttrium and rare earths in hydrothermal fluids from the Mid-Atlantic Ridge: implications for Y and REE behaviour during nearvent mixing and for the Y/Ho ratio of Proterozoic seawater. Chem. Geol. 155, 77–90.

Bekker, A., Slack, J.F., Planavsky, N., Krapez, B., Hofmann, A., Konhauser, K.O., Rouxel, O.J., 2010. Iron formation: the sedimentary product of a complex interplay among mantle, tectonic, oceanic and biospheric processes. Econ. Geol. 105, 467–508.

Beukes, N.J., 1973. Precambrian iron-formations of Southern Africa. Econ. Geol. 68, 960–1004.

Beukes, N.J., Klein, C., 1990. Geochemistry and sedimentology of a facies transition from microbanded to granular iron-formation in the early Proterozoic Transvaal Supergroup, South Africa. Precambrian Res. 47, 99–139.

Bhattacharya, H.N., Chakraborty, I., Ghosh, K.K., 2007. Geochemistry of some banded iron-formations of the Archean supracrustals, Jharkhand–Orissa region, India. J. Earth Syst. Sci. 116 (3), 245–259.
Bolhar, R., Kamber, B.S., Moorbath, S., Fedo, C.M., Whitehouse, M.J., 2004. Characterization of Early Archean chemical sediments by trace element signatures. Earth Planet. Sci. Lett. 222, 43–60.
Bolhar, R., Van Kranendonk, M.J., Kamber, B.S., 2005. A trace element study of siderite–jasper banded iron formation in the 3.45 Ga Warrawoona Group, Pilbara Craton—formation from hydrothermal fluids and shallow seawater. Precambrian Res. 137, 93–114.
Bonatti, E., 1975. Metallogenesis at oceanic spreading centers. Annu. Rev. Earth and Planet. Sci. 3, 401–433.
Boynton, W.V., 1984. Geochemistry of the REE: meteorite studies. In: Henderson (Ed.), Rare earth Element Geochemistry. Elsevier, pp. 63–114.
Campbell, A.C., Palmer, M.R., Klinkhammer, G.P., Bowers, T.S., Edmond, J.M., Lawrence, J.R., Casey, J.F., Thompson, G., Humphris, S., Rona, P., Karson, J.A., 1988. Chemistry of hot springs on the Mid-Atlantic Ridge. Nature 335, 514–519.
Chombong, N.N., Suh, C.E., 2013. 2883 Ma commencement of BIF deposition at the northern edge of Congo craton, southern Cameroon: new zircon SHRIMP data constraint from metavolcanics. Episodes 36, 47–57.
Danielson, A., Moller, P., Dulski, P., 1992. The europium anomalies in banded iron formations and the thermal history of the oceanic crust. Chem. Geol. 97, 89–100.
de Baar, H.J.W., German, C.R., Elderfield, H., Vangaans, P., 1988. Rare-earth element distributions in anoxic waters of the Cariaco Trench. Geochim. Cosmochim. Acta 52, 1203–1219.
De Carlo, E.H., Green, W.J., 2002. Rare earth elements in the water column of Lake Vanda, McMurdo Dry Valleys, Antarctica. Geochim. Cosmochim. Acta 66, 1323–1333.
Derry, L.A., Jacobsen, S.B., 1990. The chemical evolution of Precambrian seawater: evidence from REEs in banded iron formations. Geochim. Cosmochim. Acta 54, 2965–2977.
Douville, E., Bienvenu, P., Charlou, J.-L., Donval, J.-P., Fouquet, Y., Appriou, P., Gamo, T., 1999. Yttrium and rare earth elements in fluids from various deep-sea hydrothermal systems. Geochim. Cosmochim. Acta 63 (5), 627–643.
Dymek, R.F., Klein, C., 1988. Chemistry, petrology and origin of banded iron formation lithologies from 3800 Ma Isua supracrustal belt, West Greenland. Precambrian Res. 39, 247–302.
Ewers, W.E., Morris, R.C., 1981. Studies of the Dales George member of the Brockman Iron Formation, Western Australia. Econ. Geol. 76, 1929–1953.
Frei, R., Dahl, P.S., Duke, E.F., Frei, K.M., Hansen, T.R., Frandsson, M.M., Jensen, L.A., 2008. Trace element and isotopic characterization of Neoarchean and Paleoproterozoic iron formations in the Black Hills (South Dakota USA): assessment of chemical change during 2.9–1.9 Ga deposition bracketing the 2.4–2.2 Ga first rise of atmospheric oxygen. Precambrian Res. 162 (3–4), 441–474.
Fryer, B.J., 1977. Rare earth evidence in iron-formations for changing Precambrian oxidation states. Geochim. Cosmochim. Acta 41, 361–367.
Fryer, B.J., 1983. Rare earth elements in iron-formation. In: Trendall, A.F., Morris, R.C. (Eds.), Iron-Formation: Facts and Problems. Elsevier, Amsterdam, pp. 345–358.
Goodwin, A.M., 1991. Precambrian Geology—The Dynamic Evolution of the Continental Crust. Academic Press, Harcourt Brace Jovanovich Publishers, 666 p.
Gross, G.A., 1983. Iron-formation in fold belts marginal to the Ungava craton. In: Trendall, A.F., Morris, R.C. (Eds.), Iron Formation: Facts and Problems. Elsevier, Amsterdam, pp. 253–294.
Gross, G.A., McLeod, C.R., 1980. A preliminary assessment of the chemical composition of iron-formation in Canada. Can. Mineral. 18, 223–229.
Hein, J.R., Schulz, M.S., Kang, J.K., 1990. Insular and submarine ferromanganese mineralization of the Tongap-Lau region. Mar. Min. 9, 305–354.
Holland, H.D., 1984. The Chemical Evolution of the Atmosphere and Oceans. Princeton University Press, Princeton, pp. 582–$9.
Hou, K., Li, Y., Gao, J., Liu, F., Qin, Y., 2014. Geochemistry and Si–O–Fe isotope constraints on the origin of banded iron formations of the Yuanjiacun Formation, Lvliang Group, Shanxi, China. Ore Geol. Rev. 57, 288–298.
Ilouga, C.D.I., Suh, C.E., Ghogomu, R.T., 2013. Textures and rare earth elements composition of Banded Iron Formations (BIF) at Njweng prospect, Mbalam Iron Ore District, Southern Cameroon. Int. J. Geosci. 4, 146–165.
Isley, A.E., 1995. Hydrothermal plumes and the delivery of iron to banded iron formation. J. Geol. 103, 169–185.
James, H.L., 1954. Sedimentary facies of iron-formations. Econ. Geol. 49, 235–293.
Kato, Y., Yamaguchi, K.E., Ohmoto, H., 2006. Rare earth elements in Precambrian banded Fe formations: secular changes of Ce and Eu anomalies and evolution of atmospheric oxygen. In: Kessler, S.E., Ohmoto, H. (Eds.), Evolution of the Atmosphere, Hydrosphere, and Biosphere on Early Earth: Constraints from Ore Deposits. Geological Society of America, Denver.
Kato, Y., Ohta, I., Tsunematsu, T., Watanabe, Y., Isozaki, Y., Maruyama, S., Imai, N., 1998. Rare earth element variations in mid-Archean banded iron formations: implications for the chemistry of ocean and continent and plate tectonics. Geochim. Cosmochim. Acta 62, 3475–3497.
Kerrich, R., Said, N., Manikyamba, C., Wyman, D., 2013. Sampling oxygenated Archaean hydrosphere: implications from fractionation of Th/U and Ce/Ce* in hydrothermally altered volcanic sequences. Gondwana Res. 23, 506–525.
Kholodov, V.N., Butuzova, G.Y., 2001. Problems of iron and phosphorus geochemistry in the Precambrian. Lithol. Miner. Resour. 36 (4), 291–302.
Klein, C., Beukes, N.J., 1989. Geochemistry and sedimentology of a facies transition from limestone to iron-formation deposition in the Early Proterozoic Transvaal Supergroup, South Africa. Econ. Geol. 84, 1733–1774.
Klein, C., 2005. Some Precambrian banded iron-formations (BIFs) from around the world: their age, geologic setting, mineralogy, metamorphism, geochemistry, and origin. Am. Mineral. 90, 1473–1499.
Klein, C., Beukes, N.J., 1992. Time distribution, stratigraphy, sedimentologic setting, and geochemistry of Precambrian iron-formations. In: Schopf, J.W., Klein, C. (Eds.), The Proterozoic Biosphere. Cambridge University Press, Cambridge, pp. 139–146.
Klein, C., Beukes, N.J., 1993. Sedimentology and geochemistry of glaciogenic Late Proterozoic Rapitan iron-formation in Canada. Econ. Geol. 88, 542–565.
Koeppenkastrop, D., De Carlo, E.H., 1992. Sorption of rare-earth elements from seawater onto synthetic mineral particles—an experimental approach. Chem. Geol. 95, 251–263.
Kornprobst, J., Lasserre, M., Rollet, M., Soba, D., 1976. Existence au Cameroun d'un magmatisme alcalin Panafricain ou plus ancien: la syénite néphélinique de Nkonglong. Comparaison avec les roches alcalines connues dans la même région. Bull. Soc. Géol. Fr. 18 (5), 1295–1305, tome XVIII.
Lascelles, D.F., 2007. Black smokers and the Archean environment: uniformitarian model for the genesis of iron-formations. Ore Geol. Rev. 32, 381–411.
Lottermoser, B.G., Ashley, P.M., 2000. Geochemistry, petrology and origin of Neoproterozoic ironstones in the eastern part of the Adelaide Geosyncline South Australia. Precambrian Res. 101, 49–67.
Manikyamba, C., Naqvi, S.M., 1995. Geochemistry of Fe–Mn formations in the Archean Sandur schist belt, India: mixing of clastic and chemical processes at a shallow shelf. Precambrian Res. 72, 69–95.
Manikyamba, C., Balaram, V., Naqvi, S.M., 1993. Geochemical signatures of polygenetic origin of the banded iron formation (BIF) of Archean Sandur greenstone belt (schist belt), Karnataka nucleus, India. Precambrian Res. 61, 137–164.
Marchig, V., Gundlach, H., Möller, P., Schley, F., 1982. Some geochemical indicators for discrimination between diagenetic and hydrothermal metalliferous sediments. Mar. Geol. 50, 241–256.
Maurizot, P., Abessolo, A., Feybesse, J.L., Johan, L.P., 1986. Étude de Prospection Minière du Sud-Ouest Cameroun. Synthèse des Travaux de 1978 à 1985. Rapport de BRGM 85, p. 274.
McLennan, S.M., Hemming, S., McDaniel, D.K., Hanson, G.N., 1993. Geochemical approaches to sedimentation, provenance, and tectonics. In: Special Papers—Geological Society of America., pp. 21–40.
Michard, A., Albarède, F., 1986. The REE content of some hydrothermal fluids. Chem. Geol. 55, 51–60.
Michard, A., Albarede, F., Michard, G., Minster, J.F., Charlou, J.L., 1983. Rare-earth elements and uranium in high-temperature solutions from East Pacific Rise hydrothermal vent field (13°N). Nature 303, 795–797.
Michard, A., Michard, G., Stuben, D., Stoffers, P., Cheminee, J.-L., Binard, N., 1993. Submarine thermal springs associated with young volcanoes: the Teahitia vents, Society Islands Pacific Ocean. Geochim. Cosmochim. Acta 57, 4977–4986.
Mitra, A., Elderfield, H., Greaves, M.J., 1994. Rare earth elements in submarine hydrothermal fluids and plumes from the Mid-Atlantic Ridge. Mar. Chem. 46, 217–235.
Mloszewska, A.M., Pecoits, E., Cates, N.L., Mojzsis, S.J., O'Neil, J., Robbins, L.J., Konhauser, K.O., 2012. The composition of earth's oldest iron formations: the Nuvvuagittuq Supracrustal Belt (Quebec, Canada). Earth Planet. Sci. Lett. 317–318, 331–342.
Mvondo, H., den Brok, S.W.J., Mvondo Ondoa, J., 2003. Evidence for extension and exhumation of the Yaounde nappe (Pan-African fold belt, Cameroon). J. Afr. Earth Sci. 36, 215–231.
Nédélec, A., Nsifa, E.N., Martin, H., 1990. Major and trace element geochemistry of the Archaean Ntem plutonic complex (South Cameroon): petrogenesis and crustal evolution. Precambrian Res. 47, 35–50.
Nforba, M.T., Suh, C.E., Kabeyene, K.V.K., 2010. Mbalam iron ore project, northern edge of the Congo craton, southeast Cameroon. In: Goldfarb, R.J., Marsh, E.E., Monecke, E. (Eds.), Proceedings of the Society of Economic Geologists on the Challenge of Finding New Mineral Resources: Global Metallogeny, Innovative Ex-ploration and New Discoveries, SEG Extended Abstracts. Colorado, G-22.
Njinchuki, N.D., 2011. Petrographical and Geochemical Studies of Ngoa Area (Southern Cameroon): Evidence for Iron Deposit. Master Thesis. University of Yaoundé I, 74p.
Nsoh, F.E., Agbor, T.A., Etame, J., Suh, E.C., 2014. Ore-textures and geochemistry of the Nkout iron deposit South East Cameroon. Sciences. Technol. Dév. 15, 43–52.
Nzenti, J.P., Barbey, P., Macaudière, J., Soba, D., 1988. Origin and evolution of the late Precambrian high-grade Yaounde gneisses (Cameroon). Precambrian Res. 38, 91–109.
Olivarez, A.M., Owen, R.M., 1991. The europium anomaly of seawater: implications for fluvial versus hydrothermal REE inputs to the oceans. Chem. Geol. 92, 317–328.
Planavsky, N., Bekker, A., Rouxel, O.J., Kamber, B., Hofmann, A., Knudsen, A., Lyons, W.T., 2010. Rare Earth Element and yttrium compositions of Archaean and Paleoproterozoic Fe formations revisited: new perspectives on the significance and mechanisms of deposition. Geochim. Cosmochim. Acta 74, 6387–6405.
Pouclet, A., Tchameni, R., Mezger, K., Vidal, M., Nsifa, E.N., Shang, C.K., Penaye, J., 2007. Archaean crustal accretion at the northern border of the Congo craton (South Cameroon). The charnockite-TTG link. Bull. Geol. Soc. Fr. 178, 331–342.

Shang, C.K., Liégeois, J.P., Satir, M., Frisch, W., Nsifa, E.N., 2010. Late Archaean high-K granite geochronology of the northern metacratonic margin of the Archaean Congo craton, Southern Cameroon: evidence for Pb-loss due to non-metamorphic causes. Gondwana Res. 18 (2–3), 337.

Shang, C.K., Satir, M., Nsifa, E.N., Liegeois, J.P., Siebel, W., Taubald, H., 2007. Archaean high-K granitoids produced by remelting of the earlier Tonalite–Trondhjemite–Granodiorite (TTG) in the Sangmelima region of the Ntem complex of the Congo craton, southern Cameroon. Int. J. Earth Sci. 96, 817–842.

Shang, C.K., Satir, M., Siebel, W., Nsifa, E.N., Taubald, H., Liegeois, J.P., Tchoua, F.M., 2004. Major and trace element geochemistry, Rb–Sr and Sm–Nd systematics of TTG magmatism in the Congo craton: case of the Sangmelima region, Ntem complex, southern Cameroon. J. Afr. Earth Sci. 40, 61–79.

Shang, C.K., Satir, M., Siebel, W., Taubald, H., Nsifa, E.N., Westphal, M., Reitter, E., 2001. Genesis of K-rich granitoids in the Sangmelima region, Ntem complex (Congo craton), Cameroon. Terra Nostra 5, 60–63.

Shimizu, H., Umemoto, N., Masuda, A., Appel, P.W.U., 1990. Sources of iron-formations in the Archean Isua and Malene supracrustals, West Greenland: evidence from La–Ce and Sm–Nd isotopic data and REE abundances. Geochim. Cosmochim. Acta 54, 1147–1154.

Spier, C.A., de Oliveira, S.M.B., Sial, A.N., Rios, F.J., 2007. Geochemistry and genesis of the banded iron formations of the Caue Formation, Quadrilatero Ferrıfero, Minas Gerais, Brazil. Precambrian Res. 152, 170–206.

Suh, C.E., Cabral, A., Shemang, E.M., Mbinkar, L., Mboudou, G.G.M., 2008. Two contrasting iron-ore deposits in the Precambrian mineral belt of Cameroon, West Africa. Explor. Min. Geol. 17, 197–207.

Suh, C.E., Cabral, A.R., Ndime, E., 2009. Geology and ore fabric of the Nkout high-grade haematite deposit, southern Cameroon. Proceedings of the 10th Biennial of Smart Science for Exploration and Mining, 558–560.

Taylor, S.R., McLennan, S.M., 1985. The Continental Crust: Its Composition and Evolution. Blackwell, 312 p.

Tchameni, R., Mezger, K., Nsifa, N.E., Pouclet, A., 2001. Crustal origin of Early Proterozoic syenites in the Congo Craton (Ntem Complex), South Cameroon. Lithos 57 (1), 23–42.

Toteu, S.F., Van Schmus, W.R., Penaye, J., Nyobe, J.B., 1994. U–Pb and Sm–Nd evidence for Eburnean and Pan-African high-grade metamorphism in cratonic rocks of southern Cameroon. Precambrian

Toteu, S.F., Yongue, R.F., Penaye, J., Tchakounte, J., Seme Mouangue, A.C., Van Schmus, W.R., Deloule, E., Stendal, H., 2006. U–Pb dating of plutonic rocks involved in the nappe tectonic in southern Cameroon: consequence for the Pan-African orogenic evolution of the central African fold belt. J. Afr. Earth Sci. 44, 479–493.

Tsikos, H., Moore, J.M., 1997. Petrography and geochemistry of the Paleoproterozoic Hotazel Iron-Formation, Kalahari Manganese Field, South Africa: implications for Precambrian manganese metallogenesis. Econ. Geol. 92, 87–97.

Usui, A., Someya, M., 1997. Distribution and composition of marine hydrogenetic and hydrothermal manganese deposits in the northwest Pacific. In: Nicholson, K., Hein, J.R., Buhn, B., Dasgupta, S. (Eds.), Manganese Mineralization: Geochemistry and Mineralogy of Terrestrial and Marine Deposits, vol. 119. Geological Society London Special Publications, pp. 177–198.